


Review

Ultrafast Mid-IR Laser Pulses Generation via Chirp Manipulated Optical Parametric Amplification

Zuofei Hong ^{1,2} , Seyed Ali Rezvani ¹, Qingbin Zhang ^{1,*} and Peixiang Lu ^{1,2}

¹ School of Physics and Wuhan National Laboratory for Optoelectronics, Huazhong University of Science and Technology, Wuhan 430074, China; zuofei.hong@wit.edu.cn (Z.H.); ash.maison@yahoo.com (S.A.R.); lupeixiang@hust.edu.cn (P.L.)

² Laboratory of Optical Information Technology, Wuhan Institute of Technology, Wuhan 430205, China

* Correspondence: zhangqingbin@hust.edu.cn; Tel.: +86-027-8754-3755

Received: 31 March 2018; Accepted: 25 April 2018; Published: 30 April 2018



Abstract: Over the past decades, optical parametric amplification (OPA) has become one of the most promising sources of ultrafast Mid-IR laser, owing to its outstanding properties including ultrabroad bandwidth, superior tunability, good beam quality, and scalable energy. In this paper, we review the recent progress in ultrashort laser pulse generation via chirp manipulated OPA, which improves the energy scalability and gain bandwidth by strategically chirping both pump and seed pulses. The gain mechanism is theoretically analyzed and the OPA processes are numerically simulated. In addition, the concept is verified experimentally. Femtosecond pulses with hundreds of mJ are generated in a high energy dual-chirped-OPA (DC-OPA), and ultrabroadband μJ -level spectra supporting sub-2-cycle pulse durations are achieved in BBP-OPA. Furthermore, the obtained pulses show excellent tunability through the NIR to Mid-IR regions, which makes them a suitable seeding source for further amplification as well as powerful tools in various applications such as strong field physics, attosecond science, and ultrafast spectroscopy.

Keywords: ultrafast laser; strong field physics; high-order harmonic generation; optical parametric amplifier; mid-infrared source

1. Introduction

In the past decades, femtosecond laser pulses have become effective tools in various fields including high-order harmonic generation (HHG) [1–6], strong-field ionization [6–17], and time-resolved spectroscopy [18–24] due to their ultrashort pulse duration and high peak intensity. Benefiting from the Kerr lens mode-locking (KLM) [25,26] and chirped pulse amplification (CPA) [27–29], the Ti:sapphire lasers have developed rapidly towards shorter pulse durations and higher pulse energies. However, restrained by the bandwidth of the gain medium, femtosecond pulses from solid-state laser systems are mostly centered at wavelengths shorter than 1 μm , which cannot meet the requirements of potential applications.

Particularly, HHG is a well-accepted method of producing fully coherent light in the extreme ultraviolet (XUV) to X-ray regions, which utilizes femtosecond laser pulses as the driving source. During the HHG process, the maximum obtainable photon energy follows the cutoff law $E_c = I_p + 3.17 \times U_p$, where I_p is the ionization potential and U_p is the ponderomotive energy [1,30,31]. Since U_p scales with the square of the laser wavelength λ^2 , using a driving pulse with a longer center wavelength is a practical approach to the generation of harmonics with higher photon energy. Besides, the longer wavelength laser source also meets the strict requirement of tunneling ionization with the Keldysh parameter $\gamma \ll 1$, where the electron is ionized from the barrier formed by the combination of the Coulomb potential and quasi-static laser field. Moreover, using tunneling as fundamental concept,

a lot of strong field phenomena and applications such as photoelectron holography [32], electron correlation in double ionization [33,34] and molecular orbital tomography [35–38] can be interpreted or realized.

Motivated by the applications, efforts have been made to exploit ultrashort driving fields with tunable center wavelengths. Owing to the capability of producing visible (VIS) to mid-infrared (Mid-IR) pulses with high single-pass gain and ultrabroad bandwidth, optical parametric amplification (OPA) has been a promising source of tunable laser pulses in ultrafast research [39,40]. OPA is a parametric process based on the second-order nonlinearity of a crystal, during which the energy of a high-frequency pump pulse transfers to a low-frequency seed pulse through difference frequency generation (DFG). The seed pulse is amplified to the signal and the pump pulse gets depleted, meanwhile an idler pulse with the frequency of $\omega_i = \omega_p - \omega_s$ is generated. Energy conservation $\hbar\omega_p = \hbar\omega_s + \hbar\omega_i$ and momentum conservation (also known as phase-matching) $\hbar\vec{k}_p = \hbar\vec{k}_s + \hbar\vec{k}_i$ have to be fulfilled in the three-wave interactions. Comprehensive overviews on the OPA principle and its development can be found in [41–46].

In an ultrafast optical parametric amplifier, a critical limit on the gain bandwidth is the phase-mismatch (or wave-vector mismatch) $\Delta k = \vec{k}_p - \vec{k}_s - \vec{k}_i$. In order to compress the obtained pulses to ultrashort or even few-cycle durations, the phase-mismatch has to be small values for a broad range of signal/idler wavelengths. Usually, the crystal angle θ is selected to satisfy phase-matching for the center wavelengths, i.e., $\Delta k_0 = \vec{k}_{p0} - \vec{k}_{s0} - \vec{k}_{i0} = 0$, hence the phase-mismatch is calculated to the first order. As the signal frequency changes with $\Delta\omega$, the phase-mismatch becomes $\Delta k = \Delta k_1 + \Delta k_2 + \dots$, where $\Delta k_1 = -\partial k_s / \partial \omega_s \times \Delta\omega + \partial k_i / \partial \omega_s \times \Delta\omega = \Delta\omega \times (1/v_{gi} - 1/v_{gs})$.

Based on the equation, a straightforward way of obtaining ultrabroadband gain in OPA is to exploit the phase-matching bandwidth at degeneracy. Using signal and idler pulses centered at the same wavelength, phase-matching is realized to the first order and the pulses are amplified with an ultrabroad bandwidth. Degenerate OPA systems have been investigated in a number of previous works, and the possibility of producing degenerate few-cycle pulses has been confirmed theoretically and experimentally [47–57].

Despite the ultrabroad gain bandwidth, the concept of degenerate OPA can only be applied to certain center wavelengths with poor tunability due to the limit on the types of available ultrafast lasers [46]. At non-degenerate spectral regions, as the center wavelengths of signal and idler move away from degeneracy, the first-order phase-mismatch increases, which reduces the gain bandwidth severely. As discussed above, the first-order phase-mismatch Δk_1 is proportional to the group velocity mismatch (GVM) between the signal and idler pulses $\delta_{si} = 1/v_{gs} - 1/v_{gi}$. The idea of removing GVM to realize first-order phase-matching leads to the development of noncollinear OPA (NOPA) schemes [58–74]. In NOPA, the pump and seed beams enter the nonlinear crystal with a noncollinear angle α in between. As a result, the interacting pulses propagate toward different directions during the amplification, and group velocity matching between the signal and idler pulses can be met when v_{gs} is equal to $v_{gi} \times \cos\Omega$, Ω being the noncollinear angle between the two beams. Furthermore, the pulse-front tilting method has been proposed to improve the spatial overlap and the conversion efficiency in NOPA systems [75].

Note that the idler pulse in NOPA is obtained with an angular dispersion, which makes it impossible to be directly used in the following stages. Compared to the signal pulse, the idler has advantages such as a longer center wavelength and a passively stabilized carrier-envelope phase (CEP) [76]. As proposed and experimentally investigated in [76], the white-light continuum pulse from the self-phase-modulation (SPM) effect retains the same CEP as that of the input pulse. When the pump and seed are produced from the same laser source, the CEP of the idler pulse is defined by $\psi_i = -\pi/2 + \psi_p - \psi_s = -\pi$, which is stabilized passively. The CEP stability determines the shape of the electric field in ultrafast laser pulses, especially when the pulse has a few-cycle duration. Therefore, the CEP-stable idler pulses have attracted abundant attention in OPA research. In order to

obtain applicable idler pulses in NOPA, the angular dispersion of the beam has to be compensated, which requires energy-consuming procedures and complicates the system drastically [77,78].

Other than NOPA, several collinear OPA schemes have been proposed for non-degenerate pulse generation. Quasi-phase-matching (QPM) has been widely implemented in conditions where normal broadband phase-matching cannot be achieved. Using a periodically poled nonlinear crystal where the orientation of the crystalline axis inverts periodically as a function of the crystal thickness, the non-zero phase-mismatch is compensated during amplification. Few-cycle pulses, ranging from near-infrared (NIR) to Mid-IR, have been successfully generated from QPM-OPA schemes using crystals such as PPLN, PPSLT, and PPKTP, etc. [79–92].

Considering the group velocity mismatch between the three interacting pulses in OPA, we have proposed and experimentally investigated a collinear dual-crystal OPA (DOPA) scheme that compensates the group delay (GD) during amplification [93,94]. A piece of BaF₂ crystal with an inverted group velocity relationship to the BBO crystal is employed in DOPA to compensate the temporal walk-off between the pulses and thereby improve the bandwidth and efficiency of the system. As a result, tunable spectra that support few-cycle pulse durations at non-degenerate regions are obtained.

A novel frequency-domain OPA (FOPA) was proposed in [95]. Rather than amplifying the pulses in the temporal domain, FOPA employs frequency-domain amplification. Different ranges of the seed pulse are dispersed spatially, and the parametric process takes place in several pieces of nonlinear crystals that amplifies different spectral regions individually [96]. The broadband amplification results in a few-cycle Mid-IR pulse with millijoule level energy.

As an alternative to directly generating few-cycle pulses in broadband OPA, the employment of spectral broadening in a hollow core fiber (HCF) accompanied with a narrowband OPA is also a promising approach. The self-phase modulation (SPM) of an ultrashort pulse in HCF filled with gas can efficiently broaden the pulse spectrum, and after the dispersion compensation, the broadened spectrum can be recompressed to few-cycle durations. The HCF compression has manifested its validity in a number of previous research studies [97–100].

It is significant to point out that, restrained by the damage threshold of the employed components such as the nonlinear crystal, the periodically poled crystal, or the hollow core fiber, the energy scalability in the above systems are usually quite limited. The state-of-the-art Ti:sapphire laser system is capable of producing femtosecond laser pulses with the energy of hundreds of millijoules, which is difficult to be directly utilized in conventional OPA due to the above limitations. Therefore, the novel OPA schemes that might achieve better performance via manipulating the chirps of both pump and seed pulses are proposed. After temporally stretching the input pump pulse, an ultrahigh pulse energy can be fully utilized while the peak intensity of the incident beam remains lower than the damage threshold of the nonlinear crystal, hence evidently improving the energy scalability of the system. On the other hand, the possibility of individually manipulating pump and seed chirps enables one to match the central frequencies of input pulses in different slices, which is also beneficial for the system gain bandwidth. Stimulated by the recently proposed multi-plate spectral broadening scheme [101,102], an intense supercontinuum with ultrabroad bandwidth can be used to pump the OPA system that further exploits the potential of chirp manipulated OPA scheme.

In this paper, we focus on the chirp manipulated OPA scheme and review the developments utilizing this method, the structure of the paper is arranged as follows. In Section 2, the theoretical investigations on the high-energy OPA scheme are reported. In Section 3, the chirp manipulated OPA pumped by a spectrally broadened laser is analyzed and discussed. In Section 4, the latest experimental results on broadband pumped chirp manipulated OPA are presented. In Section 5, the prospects of the chirp manipulated OPA are discussed and the conclusions are drawn.

2. High-Energy Dual-Chirped-OPA (DC-OPA)

The power scalability of OPA is limited by both the pump laser energy and the size of the nonlinear crystals. In order to apply more pump energy, naturally, the concept of CPA is transferred to OPA, forming a new scheme called OPCPA. In an OPCPA, the seed pulse is first stretched to a duration that is comparable to a pump pulse with a markedly reduced peak intensity, and then a high-energy pump is used to amplify the seed. Finally a much higher amplified pulse energy than that from an OPA is obtained. In this scheme, to achieve a good temporal overlap between pump and seed pulses, one can employ a high-energy laser system with a relative long pulse duration (for example, a picosecond or nanosecond Nd:YAG system) as the pump source.

Limited by the gain bandwidth of a collinear OPCPA geometry, a picosecond pump laser usually results in a longer than 100-fs amplified signal pulse [103], which is not sufficient for many applications. To obtain a relatively short IR pulse, a noncollinear OPCPA of 1.56- μm pulses using KTA is later proposed and demonstrated [104], in which 100-fs pulses from an erbium fiber laser were stretched to 100 ps and the KTA crystals were synchronously pumped by high-power 100-ps pulses from a Nd:YLF regenerative amplifier at 1.053 μm . This work opens the door for power scaling of OPCPA to simultaneously obtain a high peak power and an ultrashort pulse duration less than 100 fs. Following this pioneering work, Mucke et al. [100] have demonstrated a 4-stage KTP/KTA OPCPA, which produce a CEP-stable multi-mJ 1.5- μm \sim 70-fs pulse based on the fusion of a diode-pumped solid-state (DPSS) femtosecond Yb:KGW MOPA system and picosecond Nd:YAG solid-state technology. Even if the abovementioned works show the ability of generating IR output energy reaches the multi-mJ level in OPCPA, OPCPA in general faces important technical challenges [42], such as the requirement of a specific pump laser, the difficulty in synchronization with an external pump laser, and the unwanted generation of parasitic superfluorescence accompanying the primary pulse in broadband high-parametric-gain configurations [105].

Keep in mind that how much pump energy can be applied is actually determined by whether the peak pump intensity exceeds the damage threshold of a nonlinear medium. In an OPA, although periodically poled nonlinear crystals such as LiNbO₃ (PPLN) and stoichiometric LiTaO₃ (PPSLT) have high nonlinearity with high conversion efficiency, the available pump intensity in such OPA is quite low owing to the low damage threshold of the crystal and its AR coatings. Therefore, OPA with PPLN and PPSLT crystals might be suitable for generating ultrashort pulse durations with moderate pulse energy but promising for high repetition rates (>1 kHz). On the other hand, beta-BaB₂O₄ (BBO) is one of the most outstanding nonlinear optical crystals for obtaining broadband IR pulses, which has unique properties: a wide transparency region (0.19–3.5 μm), wide phase-matching range (0.41–3.5 μm), large nonlinear coefficient, and high damage threshold. In the OPA scheme with BBO, an output energy up to 7 mJ with a pulse width of 40 fs [106] was achieved at a signal wavelength near 1.4 μm using a terawatt Ti:sapphire laser system 0.8 μm . In this work, the pump intensity is already close to the crystal damage threshold, a further increase in the output power of the OPA must enlarge the aperture of the BBO crystals. However, the power scalability of the OPA is limited by the available aperture size of the BBO crystals (typically $\sim 20 \times 20 \text{ mm}^2$). On the other hand, a BBO OPA pumped by 800-nm pulses can easily produce a few-cycle IR pulse with a multi-mJ output energy. Since the maximum output is limited by the damage threshold of the BBO crystals, the power scalability for the pump laser is inferior to that of the OPCPA. Although Ti:sapphire laser systems with >100 TW peak power and 10 Hz repetition rate are already available, they cannot be applied in an OPA as they stand owing to the damage threshold of the BBO crystals. Moreover, the concept of OPCPA does not work if we employ a high-energy Ti:sapphire laser. If we only stretch the seed pulse in OPCPA, the intensity of the pump pulse from the high-energy Ti:sapphire laser is still far beyond the crystal damage threshold. If a Ti:sapphire laser with sufficient energy can be applied to pump an OPA while preventing damage to BBO crystals, we will conveniently obtain a high IR energy.

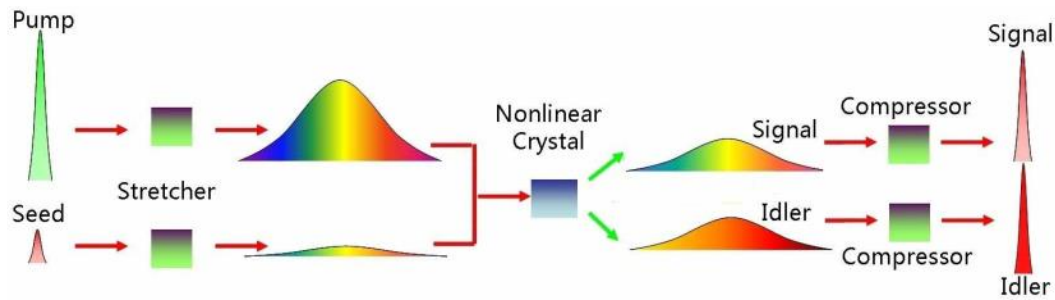


Figure 1. Scheme of dual-chirped optical parametric amplification (DC-OPA).

To this end, a dual-chirped OPA (DC-OPA), which simultaneously obtains high peak power and ultrashort pulse duration in the IR region, is proposed in [107] and shown in Figure 1. The DC-OPA is seeded with a chirped, broadband seed pulse and pumped by a stretched, broadband pump pulse. In our envisaged DC-OPA system, automatically synchronized pump and seed pulses are obtained because they come from a common source. The pump pulse can be spatially separated into two pulses on a beam splitter, one strong and the other one weaker. The strong one will be used as a pump pulse, and the weaker one will be used to generate the seed pulse via white-light generation, e.g., in a sapphire plate.

Figure 2 shows the dependence of conversion efficiency and bandwidth for output signal on the GDD values of seed pulses. The pump pulse at 800 nm has a Gaussian temporal profile with a duration of 35 fs that is stretched to 792 fs by adding a GDD of $-10,000 \text{ fs}^2$. The added GDD values of 35-fs seed pulse at 1400 nm are varied by a step of 2000 fs^2 . Under a pump intensity of $100 \text{ GW}/\text{cm}^2$ and a designed energy gain of 10^3 , it is found that the optimized seed GDD ranges from 3000 fs^2 to 5000 fs^2 for signal pulse (Figure 2a) and 3500 fs^2 to 5500 fs^2 for idler pulse (Figure 2b). Relatively high total conversion efficiency (over 40%) with a broad bandwidth supporting a sub-40-fs signal and idler pulses can be obtained, when we choose the proper GDD values (Pump: $-10,000 \text{ fs}^2$; Seed: $+4000 \text{ fs}^2$) for avoiding gain by narrowing and maintaining good temporal overlap.

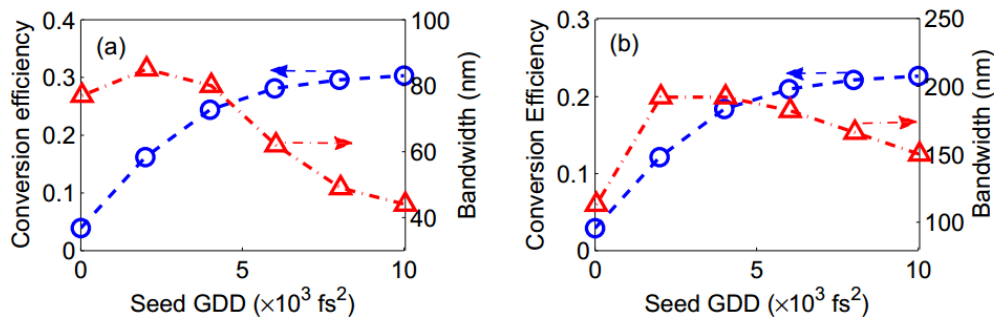


Figure 2. Signal pulse conversion efficiency (blue circle) and bandwidth (red triangle) from the DC-OPA with respect to the seed GDD ($0-10,000 \text{ fs}^2$). (a) Type-I and (b) Type-II phase matching. The conversion efficiency and bandwidth are calculated at the gain saturation point in the BBO crystal.

Before recompression of the signal and idler pulses, it is essential to know their spectral properties. We chose a set of GDD values (pump: $-10,000 \text{ fs}^2$, seed: 4000 fs^2) within the optimized range to treat this issue. It is shown in Figure 3a that an amplified signal pulse at $1.4 \mu\text{m}$ exhibits a smooth distribution with a bandwidth of 79 nm, which is just slightly narrower than the injected spectra of the seed pulse. Furthermore, it maintains a good beam quality for the signal pulse, as shown by the inset plot. After phase compensation, the pulse duration of the obtained signal is 40 fs (Figure 3b), which is the inset plot for the spatial profile of the obtained signal. At present, the 10 TW-class (e.g., 40 fs, 0.4 J) Ti:sapphire laser system is commercially available. From the conversion efficiency of DC-OPA, if we apply all the laser energy (0.4 J) for DC-OPA with an optimized GDD condition, we can expect

to generate more than 100 mJ signal energy before compression. Although our estimation does not include an optical loss by compressor, we will obtain more than enough TW IR laser power. Using the concept of DC-OPA, a total output energy of 1.4 μm (signal) and 1.9 μm (idler) of 210 mJ has recently been experimentally realized [108], pumped by a 700-mJ Ti:sapphire laser source.

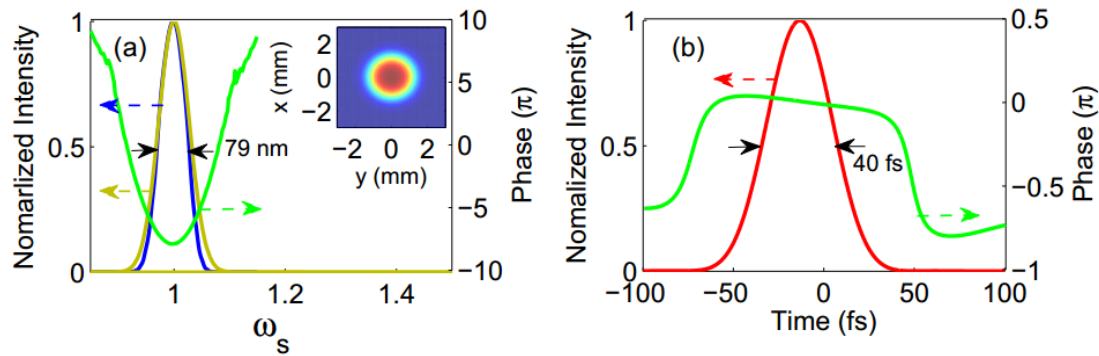


Figure 3. (a) Spectra of injected seed pulse (yellow solid line), and spectra of amplified signal pulse phase (blue solid line) together with its phase (green solid line) before phase compensation, ω_s is the signal frequency divided by its center frequency. Inset: Calculated spatial profile for the obtained signal pulse. (b) Temporal profile (red solid line) and phase (green solid line) of the amplified signal pulse after phase compensation.

3. Theory on Broadband Pumped OPA

In order to further broaden the bandwidth obtained from DC-OPA, the broad bandwidth of a comparatively lower energy Ti:sapphire laser can be helpful in such a case. In this section, we discuss the physics in the DC-OPA system pumped with a spectrally broadened pulse from a multi-plate system [109]. We attend to and focus upon how the spectral-temporal manipulation of broadband pump and seed pulses affect the gain mechanism during the parametric amplification.

The OPA process is in principle the amplification of the initial signal and idler pulses through the three-wave interaction. Therefore, the achievable output bandwidths are limited by the initial bandwidths of the seed and idler pulses. The initial signal bandwidth is defined by the input seed continuum, while the initial idler bandwidth is the bandwidth obtained in the very beginning of the amplification. In an infinitely thin layer of the nonlinear crystal, the idler pulse is produced as the DFG happens between the input pump and seed pulses. The idler bandwidth in such a crystal is not affected by the phase-matching condition but by the present pump and seed wavelengths. In further propagation through the nonlinear crystal, the gain bandwidth of both signal and idler pulses is influenced by the phase-matching condition between the three interacting pulses.

Regarding DC-OPA, the instantaneous wavelengths of the initial pump and seed can be individually manipulated, which gives us more degrees of freedom compared to conventional OPCPA, as the pump chirp is variable as well as the seed. Consequently, the system performance is largely dependent on the instantaneous wavelengths of the input pump and seed pulses. In the following, we will discuss the gain mechanism in the chirp manipulated OPA for signal and idler pulses respectively.

3.1. Gain Mechanism of Signal Pulse

With a given initial seed, the gain bandwidth of the signal pulse is mainly determined by the phase-matching condition, which in the case of DC-OPA, depends on the initial bandwidth and chirp of the input pump and seed pulses. As previously investigated in various works [110–114], the chirp-compensation scheme is favorable in such conditions. Here, we investigate the chirp-compensation scheme in the NIR to Mid-IR spectral region and the result is depicted in Figure 4. The pump and seed wavelengths cover 740–860 nm and 1000–1800 nm respectively,

and a BBO crystal cut at $\theta = 20^\circ$ is employed. The phase-matching efficiency is given by $\text{sinc}^2(\Delta kL/2)$, where $\Delta k = \vec{k}_p - \vec{k}_s - \vec{k}_i$ is the phase-mismatch and $L = 2 \text{ mm}$ is the crystal thickness.

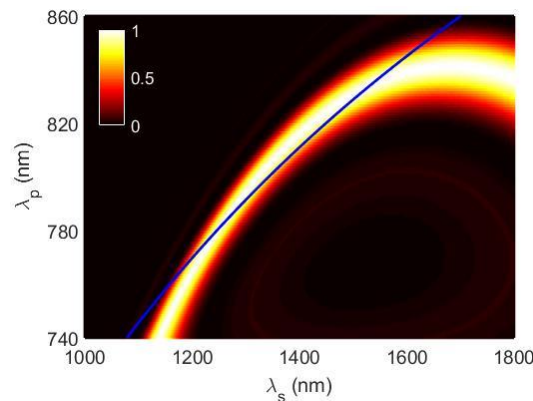


Figure 4. Phase matching efficiency with respect to the pump and seed wavelengths in a $\theta = 20^\circ$ BBO crystal, the blue line denotes the linear chirp-compensation fitting.

As observed in the figure, signal wavelength components spanning 1100–1700 nm can be phase-matched to pump wavelength components in the 740–860 nm range, and the relationship of the phase-matched pump-signal wavelengths is almost linear in this range. When pump and seed pulses of enough bandwidths are injected into the BBO crystal with the appropriate chirps, broadband phase-matching can be expected with a linear chirp-compensation fitting.

The instantaneous frequency of the interacting pulses in a chirp manipulated OPA can be expressed as follows:

$$\omega_p(t) = \omega_{p0} + C_p t \tag{1}$$

$$\omega_s(t) = \omega_{s0} + C_s t \tag{2}$$

$$\omega_i(t) = \omega_p(t) - \omega_s(t) = \omega_{i0} + C_i t \tag{3}$$

in which $\omega_m(t)$ ($m = p, s,$ and i) is the time-dependent frequency of the pump, signal, and idler pulses, respectively, ω_{m0} [rad] is the central angular frequency and C_m [rad/fs] is the temporal chirp of each pulse, $C_i = C_p - C_s$. The linear chirp-compensation fitting is denoted as the blue line in Figure 1, the line is slightly curved because of the reciprocal relationship between the wavelength λ and the angular frequency ω , the “linear” fitting actually refers to the linear chirp of the frequency, i.e., C_m being a constant value. In order to obtain phase-matching for as many signal wavelengths as possible, a pump-to-seed chirp ratio $A = C_s/C_p = 1.8$ is selected. The feasibility of the chirp-compensated OPA scheme will be experimentally verified in the following section.

3.2. Gain Mechanism of Idler Pulse

According to the above illustrations, the gain mechanism of the idler pulse is dependent on not only the instantaneous wavelengths of the input pulses, but also on the phase-matching condition during the propagation. Firstly, we investigate how the pump and seed chirps affect the initial idler bandwidth in the infinitely thin crystal. The seed pulse is stretched to a duration of 60 fs and pump pulses with different bandwidths are stretched to a same duration of 50 fs. The seed pulse with a TL duration of 13 fs is stretched with a negative GDD of -180 fs^2 . The pump pulses with TL durations of 10 fs, 20 fs, 30 fs, and 50 fs are stretched with GDDs of $\pm 90 \text{ fs}^2$, $\pm 165 \text{ fs}^2$, $\pm 215 \text{ fs}^2$, and 0 fs^2 , respectively.

The time-dependent frequencies of the initial pump, seed, and idler pulses are plotted in Figure 5. Figure 5a denote the frequencies when both the input pulses are negatively chirped, and Figure 5b denote the frequencies when the pump pulse is chirped positively the while seed pulse is chirped negatively. In order to stretch different pump pulses to the same duration, a larger pump chirp C_p

is required for a pump pulse with broader bandwidth, which explains the slopes of different solid lines in Figure 5. As given above, the temporal chirp of idler C_i is equal to $C_p - C_s$. Now that the seed chirp C_s is fixed at a negative value (dashed line in Figure 5), C_i becomes $C_p + |C_s|$, which means that a larger positive C_p corresponds to a larger C_i . By comparing the dotted lines in Figure 5a,b, it is easily seen that the TL = 10 fs pump pulse with a GDD of 90 fs² (black solid line in Figure 5b) has the largest temporal chirp among all the studied case, hence resulting in the largest idler chirp as the black dotted line in Figure 5b.

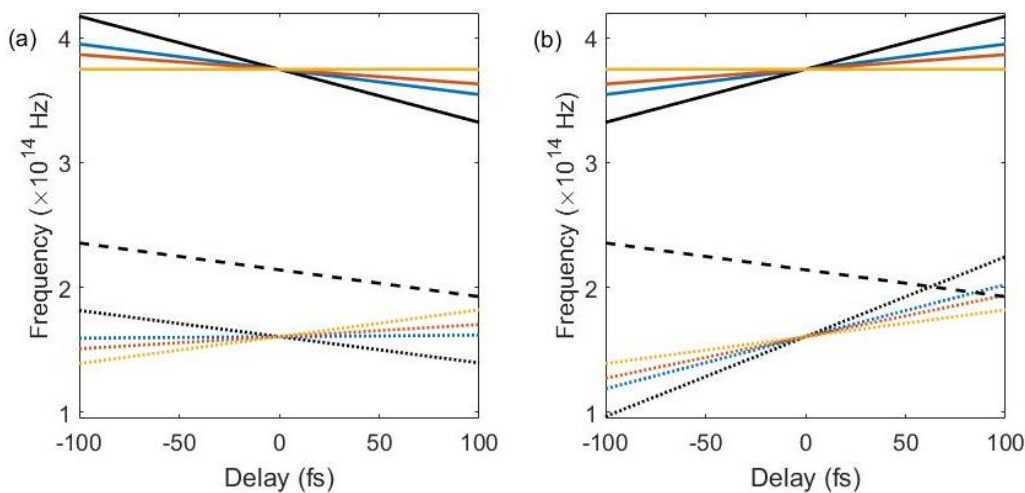


Figure 5. (a) Time-dependent frequencies of pump (solid lines), signal (dashed line), and idler (dotted lines) when the pump and seed pulses are chirped with GDDs of the same sign. (b) Time-dependent frequencies of pump (solid lines), signal (dashed line), and idler (dotted lines) when the pump and seed pulses are chirped with GDDs of opposite signs. The black, blue, red, and yellow lines represent pump pulses with TL durations of 10 fs, 20 fs, 30 fs, and 50 fs, respectively.

The initial idler pulse is produced in a time window where the input pump and seed pulses are temporally overlapped. Since the pump and seed pulses have similar durations after being chirped in all cases, the durations of the initially generated idler are also similar. According to the equation $\omega_i(t) = \omega_{i0} + C_i t$, when the idler duration is fixed, the major factor that decides the idler bandwidth becomes its temporal chirp. As a result, the broadest initial idler bandwidth is obtained with oppositely chirped pump and seed pulses.

As the initial pulses further propagate in the crystal, the nonlinear interaction between the pulses begins, during which the phase-matching condition plays an important role in deciding the idler performances. The phase-matching efficiency with respect to the pump chirp and idler wavelength is shown in Figure 6, the seed pulse is still chirped with a negative GDD of -180 fs². The initial idler bandwidth is included in the figure as the white dotted lines for reference, the bandwidth is defined as the wavelength components inside the temporal window of -50 fs $\leq t \leq 50$ fs. Since the temporal durations of all initial idler pulses are the same, this definition is a reasonable standard for the idler bandwidth comparison. Pump pulses with TL durations of 10 fs, 20 fs, 30 fs, and 50 fs are marked by the black, blue, red, and purple lines, respectively. All pump pulses are stretched to ~ 50 fs, and the line lengths stand for the idler bandwidths in each case.

Regarding the phase-matching efficiency, the bottom half of Figure 6 where the pump and seed pulses are chirped with the same sign is preferred, in which high efficiency phase matching can be achieved for a bandwidth up to 300 nm. The maximum phase-matching bandwidth is realized with a pump GDD of -40 fs², which is equivalent to the aforementioned linear fitting to the chirp-compensation scheme. Nevertheless, limited by the range of the white lines, the initial idler spectrum starts from >1700 nm, restraining the idler gain bandwidth to <200 nm.

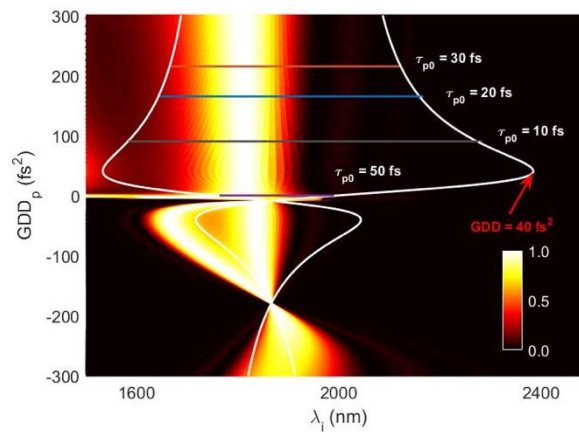


Figure 6. Phase-matching efficiency at different idler wavelengths and pump GDDs. The white lines represent the idler bandwidth within the temporal range of $-50 \text{ fs} \leq t \leq 50 \text{ fs}$. The black, blue, red, and purple lines indicate the pump pulses when their TL durations are 10 fs, 20 fs, 30 fs, and 50 fs respectively.

Comparatively, the high efficiency phase-matching bandwidth is slightly narrower in the top half of Figure 6 where the pump and seed pulses are oppositely chirped. However, the moderately phase-matched bandwidth in such condition is much broader. It is worth mentioning that phase-matching in OPA is an accumulated effect during the process, even though the perfect phase-matching bandwidth is slightly narrower. As long as the crystal angle and thickness are selected appropriately, the amplified components with moderate phase-matching still cover a broad range.

It is also observed that the phase-matching efficiency is barely affected by the pump GDD in the top half of the figure, which makes the initial idler bandwidth the decisive factor that determines the output idler bandwidth. Corresponding to Figure 5b, a pump pulse of 10-fs TL duration is capable of generating the broadest idler spectrum in the four conditions. The potentially largest bandwidth for idler is obtained with a pump GDD of 40 fs^2 , a pump bandwidth supporting a TL duration of 4.5 fs is required in this case. With the state-of-the-art technique, multi-microjoule Ti:sapphire laser pulses with even broader bandwidth are readily available [102]. Idler pulses with simultaneously optimized bandwidth and efficiency can be expected using such a pump pulse.

3.3. Simulations on BBP-OPA

The performance of broadband-pumped chirp-manipulated OPA (referred to as BBP-OPA in the following text for simplicity) is quantified by numerically simulating the process with coupled-wave equations. Various pump bandwidths and chirps are studied for a thorough comparison. Details on the numerical model can be found in [107,109]. The output signal and idler pulses are characterized by the full width at $1/e^2$ maximum (FW1/ e^2 M) bandwidth and energy-bandwidth product (EBP). Pump pulses with the energy of $300 \mu\text{J}$ and TL durations of 10 fs, 20 fs, 30 fs, and 50 fs are employed. For simplicity in the following illustrations, the TL = 50 fs pump is referred to as the narrowband pump (NBP, although its bandwidth is considerably broad), as opposed to the broadband pump (BBP) with TL durations less than 30 fs. Since the current bandwidth broadening techniques inevitably stretch the femtosecond pulses, the pump will be used as positively chirped pulses, with the designed durations ranging from 50 fs to 120 fs. The 1400-nm seed pulse is obtained from our previous experiment [94], with a FWHM bandwidth of $>200 \text{ nm}$ and the energy of $\sim 1 \mu\text{J}$. The seed pulse is chirped with a negative GDD of -180 fs^2 .

The simulation results are compared in Figure 7. As seen from the triangles in the figure, the signal bandwidth barely changes with different pump bandwidths, and the signal EBP even decreases when a broader pump bandwidth is employed. Nevertheless, in accordance to the above analysis, the BBP is evidently beneficial to the idler bandwidth and efficiency when the input pump and seed

pulses are oppositely chirped. The larger pump bandwidth increases both the idler bandwidth and EBP in Figure 7.

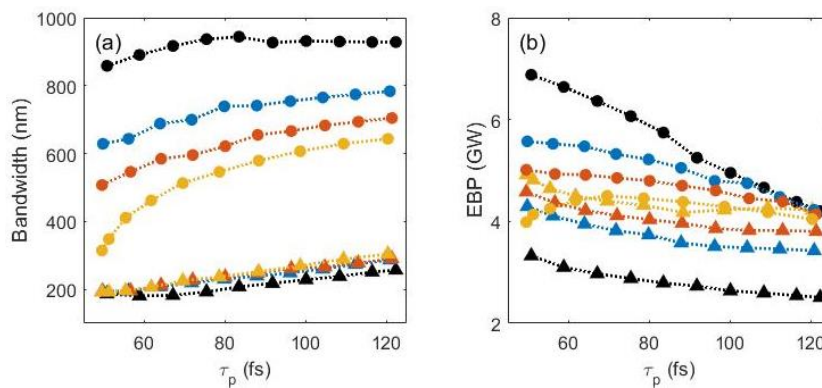


Figure 7. (a) Bandwidth and (b) energy-bandwidth product (EBP) variations of signal (triangles) and idler (circles) pulses with respect to the duration of the stretched pump pulses. The black, blue, red, and yellow lines denote pump pulses with TL durations of 10 fs, 20 fs, 30 fs, and 50 fs, respectively.

With a longer stretched pump duration, the gain narrowing is less affective to the process, resulting in broader output bandwidths. Meanwhile, the longer pulse duration indicates a lower pump peak intensity, thus realizing lower conversion efficiencies and EBPs. The highest EBP is achieved with a BBP pulse when its stretched to 50 fs, the idler spectrum with 858-nm bandwidth is obtained with a EBP of 6.9 GW, which is an impressive improvement compared to the 314-nm bandwidth and 4.0-GW EBP. The 72.6% higher EBP is mainly originated from the broader idler bandwidth and shorter TL duration.

The signal and idler spectra obtained with pump pulses stretched to 50 fs are presented in Figure 8. The input seed spectrum is plotted in Figure 8a, and the idler spectrum from an unchirped BBP-OPA is plotted in Figure 8b as the dashed lines for comparison. As shown in Figure 7a, the output signal bandwidths are similar with different pump bandwidth, hence only one spectrum is plotted as an example. The identical stretched pump duration is selected to ensure similar conversion efficiency for all systems, so the system performance can be directly revealed by the idler bandwidth. A BBO crystal with 2.5-mm thickness is used in all cases.

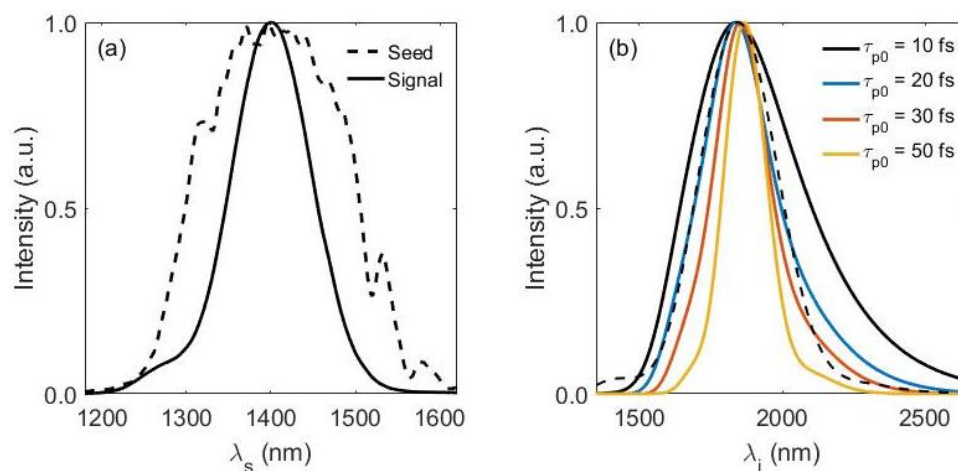


Figure 8. (a) Input (dashed line) and output (solid line) spectra of the signal. (b) Output spectra of idler pulses from systems with different pump bandwidths. Idler spectrum from an unchirped OPA (black dashed line) is plotted for comparison.

It is observed that the signal experiences gain-narrowing effect during the process, which results in ~100-nm narrower bandwidth than the initial seed. On the contrary, owing to the opposite GDDs of pump and seed pulses, the idler pulses are obtained with a much broader bandwidth compared to the signal. Not only do the idler bandwidth increase with the pump bandwidth in Figure 8b, the one from chirp-manipulated system is also much broader than the unchirped case, indicating the validity of the BBP-OPA in broadening the idler bandwidth.

Moreover, the tunability of the BBP-OPA is investigated and the results are plotted in Figure 9. The phase-matching efficiency in the BBP-OPA scheme is insensitive to the center wavelengths of the signal and idler pulses. As a result, idler pulses tunable from the NIR to Mid-IR regions can be obtained with over 600-nm bandwidth. The conversion efficiencies and TL durations of the tunable idler pulses are plotted in Figure 9b. All idler spectra can support TL durations of less than 9 fs, corresponding to <1.5 optical cycles, meanwhile a conversion efficiency of >14% can be achieved. Note that the nonlinear crystal selected here is BBO, which has strong absorption in the Mid-IR range. However, the presented concept of chirp manipulation in OPA is not limited by the crystal, therefore the BBP-OPA scheme shows great potential for the generation of few-cycle Mid-IR pulses in non-degenerate regions.

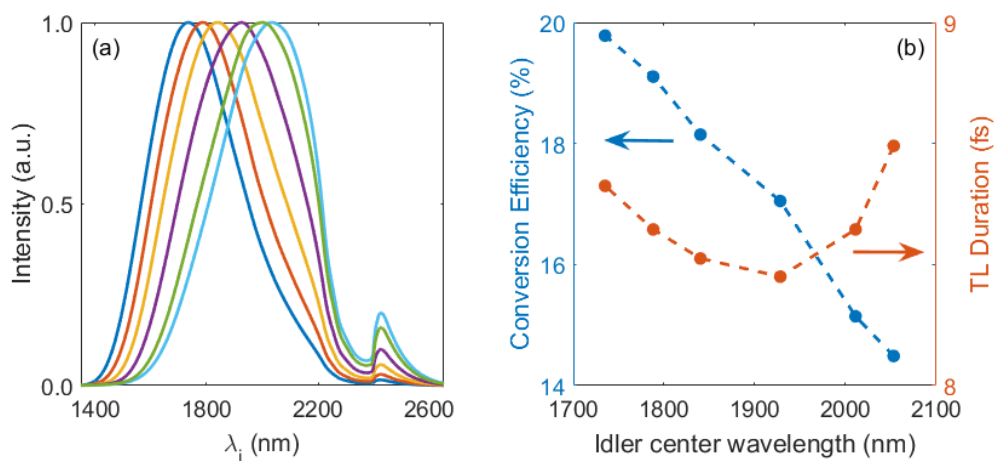


Figure 9. (a) Tunable idler spectra centered at 1730 nm (blue), 1790 nm (red), 1840 nm (yellow), 1920 nm (purple), 1990 nm (green), and 2050 nm (cyan). (b) Conversion efficiencies and TL durations of the tunable idler pulses.

4. Experiments on Broadband Pumped DC-OPA

In this section, we present the experimental results on the chirp-manipulated OPA system pumped by a spectrally broadened Ti:sapphire laser. The NIR seed and Mid-IR idler pulses are investigated separately.

4.1. BBP-OPA in NIR Region

The experimental setup of NIR BBP-OPA is depicted in Figure 10. A 800-nm Ti:sapphire femtosecond laser system (Legend Elite Duo - COHERENT.inc, US) with a pulse duration of 35 fs and energy of 300 μ J is employed. The NBP is focused by a $f = 1.3$ m convex lens and sent into an array of 4 fused silica (FS) plates for spectral broadening based on self-phase modulation effect in the plates. The position and angle of incidence of the FS plates are carefully adjusted to the realized maximum spectral bandwidth for the pump pulse. The 210- μ J BBP is obtained with a FWHM bandwidth of 73 nm, which is 2.7 times broader compared to the NBP (27 nm). The seed pulse is generated from white light continuum (WLC) in a 3-mm sapphire crystal. The BBP and WLC are synchronized and combined in a piece of 2.4-mm BBO crystal cut at $\theta = 20^\circ$. The phase-matching condition is optimized for a signal centered at 1400 nm, as shown in Figure 4. A very small noncollinear angle between the pump and seed beams is employed for the convenience of separating the output pulses.

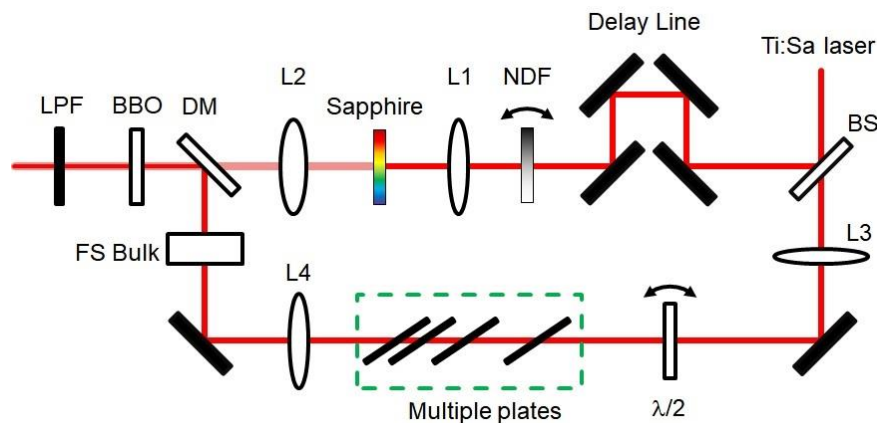


Figure 10. Schematic design of broad band pumped-OPA (BBP-OPA) in the NIR region.

The BBP is characterized with a second harmonic generation frequency-resolved optical gating (SHG-FROG), and the results are shown in Figure 11. The FWHM bandwidth of the pump spans 770–850 nm range, which is broad enough to support high-efficiency phase-matching for signal components from 1170 nm to 1660 nm according to Figure 4. The measured pump pulse duration is 87 fs, with a near-quadratic spectral phase (green dashed line in Figure 11b) corresponding to a GDD of 450 fs^2 . The seed GDD is around 240 fs^2 resulted from the transmissive optical components on the path, setting the pump-seed chirp ratio $A = C_p/C_s$ at 1.8 and a broadband signal is therefore expected.

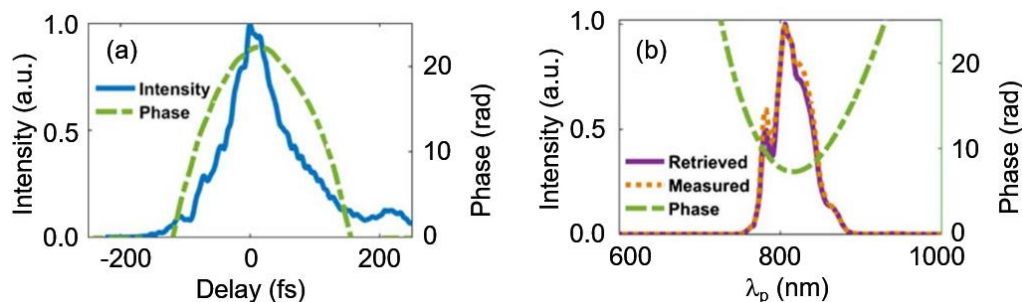


Figure 11. Spectral-temporal properties of BBP pulse. (a) Intensity (blue line) and temporal phase (green dashed line) of the pulse. (b) Retrieved (purple line) and measure (red dotted line) spectrum and spectral phase (green dashed line).

The amplified signal spectrum is plotted as the red line in Figure 12a, covering the 1000–2000 nm range with a FWHM bandwidth over 400 nm. The signal spectrum from NBP-OPA system is measured and shown as the blue line in Figure 12a, and the achieved FWHM bandwidth is only 141 nm. The difference between the spectra can be well explained by the analysis based on Figure 4. According to the chirp-compensation theory, more signal wavelength components can be phase matched with more pump wavelengths. Since the BBP has a 2.7 times broader bandwidth than the NBP, it is reasonable to realize a signal bandwidth from the BBP system that is $400/141 \approx 2.8$ times broader than the signal from the NBP system.

As mentioned above, high wavelength tunability is also expected from the BBP-OPA, therefore it is further investigated and plotted in Figure 12b. The signal wavelength is tuned by slightly rotating the BBO crystal and changing the pump-seed delay, which is equivalent to shifting the blue line in Figure 1 so that the high efficiency phase-matching wavelength is adjusted. The signal spectra in Figure 12b reveal high tunability throughout the non-degenerate NIR region from 1100 nm to 1500 nm, meanwhile the broad bandwidth is preserved.

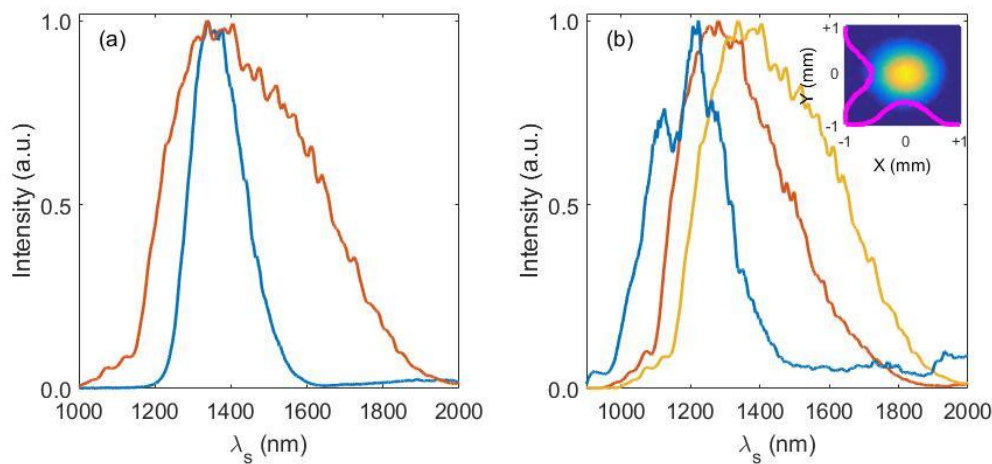


Figure 12. (a) Signal spectra obtained from NBP-OPA (blue) and BBP-OPA (red). (b) Signal spectra centered at 1200 nm (blue), 1300 nm (red), and 1400 nm (yellow). Inset: beam profile of the output signal.

Using identical pump pulse energy (180 μJ), the conversion efficiencies in BBP-OPA and NBP-OPA are both $\sim 3\%$, and the energy stability of $<1\%$ RMS is achieved for signal from BBP-OPA over 3 h. The beam quality is measured by loosely focusing the output signal into a 5-megapixel CCD camera and the beam profile is shown as the inset in Figure 12. The cross-sections of the beam on x and y axes both show an excellent Gaussian profile, which makes it a suitable laser source for successive amplification stages or further applications.

The temporal properties of the signal pulse are measured with a SHG-FROG and the results are shown in Figure 13. The uncompressed pulse duration of 34 fs is obtained with a GDD of 240 fs^2 . The obtained signal spectrum supports a sub-2-cycle TL pulse duration as short as 7.5 fs, which is plotted in Figure 13a. According to the near-quadratic spectral phase in Figure 13b, the pulse is linear-temporal-chirp dominant, which can be compressed to a near TL duration using various approaches such as prisms, gratings, chirped mirror pairs, or acoustic-optic programmable dispersive filter (AOPDF) accompanied by a bulk material.

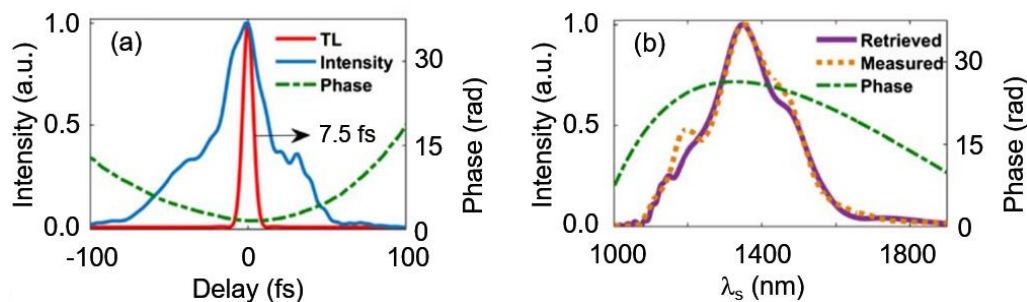


Figure 13. Spectral-temporal properties of uncompressed signal pulse. (a) Intensity (blue line), phase (green dashed line) of the pulse, and TL pulse profile (red line). (b) Retrieved (purple line) and measure (red dotted line) spectrum and spectral phase (green dashed line).

4.2. Preliminary Results on Mid-IR BBP-OPA

Despite the ultrabroad bandwidth and excellent tunability of BBP-OPA in the NIR region, the signal wavelength is inherited from the white light continuum. Since the WLC can only be extended to $\sim 2 \mu\text{m}$ [50], it is technically difficult to directly amplify the WLC and obtain broadband pulses centered at $>1.6 \mu\text{m}$. In this case, the idler pulse with longer wavelength and passive CEP stability can be utilized for further investigation. The schematic design of the BBP-OPA system for generating Mid-IR pulses is presented in Figure 14. The main difference between this system and

the previous one is that instead of using a positively chirped BBP pulse, a pair of chirped mirrors is employed to introduce negative GDD to the BBP, therefore a broadband Mid-IR idler can be expected according to the theoretical analysis. Furthermore, the recollimation of BBP is accomplished by a silver-coated concave mirror instead of a convex lens (L4 in Figure 10) in order to avoid undesired temporal and spatial distortions.

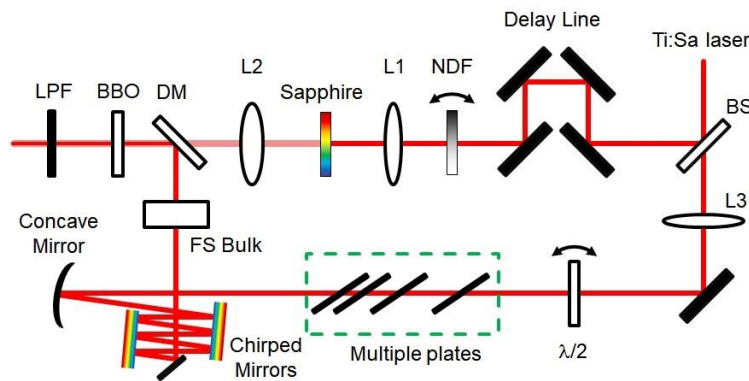


Figure 14. Schematic design of BBP-OPA in the Mid-IR region.

According to the theory, unlike the signal pulse, the idler pulse in chirp-manipulated OPA is more sensitive to the initial pump parameters. Taking that into account, we will study the idler property with various pump chirps in this section, which is realized by inserting a bulk FS material on the pump path for adjustable positive GDDs. In this way, the GDD of both NBP and BBP can be precisely manipulated by using a bulk FS of different thickness or rotating the material. In this proof-of-principle experiment, the preliminary results are obtained using NBP and BBP pulses chirped with a similar GDD around -400 fs^2 .

The pump energy of $100 \text{ } \mu\text{J}$ is used in both cases. Owing to the optimization of the pump quality, the conversion efficiencies in the NBP and BBP systems are both enhanced compared to the previous experiment. Output signal energies of $6.0 \text{ } \mu\text{J}$ and $5.6 \text{ } \mu\text{J}$ and idler energies of $3.8 \text{ } \mu\text{J}$ and $3.4 \text{ } \mu\text{J}$ are obtained in NBP and BBP systems, respectively. The higher efficiency is achieved in NBP-OPA due to the higher peak intensity of the pump pulse.

Even though the efficiency in BBP-OPA is slightly lower, the achieved bandwidth can easily compensate the energy loss. As plotted in Figure 15, the signal spectra from two systems are similar, whereas the idler spectra show an observable difference. The idler bandwidth from NBP-OPA is only 175 nm , and the idler bandwidth from BBP-OPA reaches 434 nm , which is 2.5 times larger than NBP-OPA. The spectrum is measured up to 2100 nm due to the limitation of available spectrometer (Ocean Optics NIRQuest512-2.2) in our lab. The ultrabroad bandwidth of the idler supports a sub-2-cycle TL pulse duration of 10.6 fs , which makes it a much more useful tool than the idler from NBP-OPA in potential applications, despite its slightly lower pulse energy.

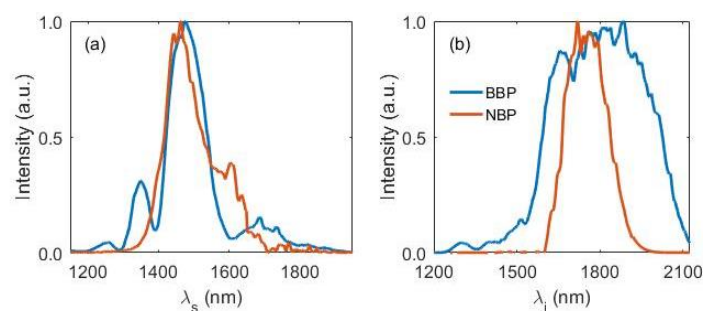


Figure 15. (a) Signal spectra obtained from NBP-OPA (red line) and BBP-OPA (blue line). (b) Idler spectra obtained from NBP-OPA (red line) and BBP-OPA (blue line).

5. Prospects and Conclusions

The BBP-OPA scheme has been proven capable of generating microjoule broadband tunable pulses in the IR region. More detailed results will be needed to further confirm this concept. Meanwhile, the potential of the proposed scheme is not limited to the present results. Broadband pump pulses with energy from several tens microjoule to the millijoule level has been realized with various techniques including the multi-plate scheme and HCF compression. Utilizing such pulses in a BBP-OPA scheme enables the generation of a more intense supercontinuum that supports few-cycle pulse duration.

On the other hand, the achieved spectra are limited to 2100 nm due to the spectrometer in our lab. Since the idler bandwidth is insensitive to the phase-matching condition, tuning the idler frequency as well as the signal is feasible by simply rotating the nonlinear crystal and changing the pump-seed delay. Considering the absorption of BBO crystal in the Mid-IR region, other nonlinear crystals such as AGS, LN or LT can be introduced owing to their higher transmission range up several microns, which will allow more efficient conversion in the Mid-IR spectral region.

The ultrashort pulses generated from chirp manipulated OPA can be a powerful tool in a number of related researches owing to its unique characteristics over commercially available Ti:sapphire lasers, including longer carrier wavelength, broader spectral bandwidth, and shorter pulse duration. The low requirement on a multi-plate scheme allows BBP generation with a wide variety of initial laser energy of only several tens to hundreds μJ . With the reported conversion efficiency, μJ -level few-cycle Mid-IR pulses can be directly obtained from a single-stage BBP-OPA pumped by a laser system with moderate pulse energy, which can benefit applications that do not require the ultrahigh energy of femtosecond laser pulses [115–119].

In particular, femtosecond IR pulses have been widely employed in ultrafast spectroscopy to investigate the carrier dynamics in semiconductor structures using pump-probe measurements [120–122]. Due to the wavelength tunability of chirp manipulated OPA accompanied with the ultrashort pulse duration, the generated pulses with lower photon energy compared to Ti:sapphire laser can be helpful in probing the carrier relaxation process. The widely variable photon energy provided by the tunable Mid-IR laser might uncover essential information about the evolution during the decay of excited states at different energy levels.

In conclusion, we introduced the chirp manipulated optical parametric amplification scheme in this paper and reviewed some of the results on the latest developments. The superb energy scalability of DC-OPA is a promising route to fully utilize the hundreds millijoule energy of a Ti:sapphire laser in an OPA system. In addition, the dual-chirped geometry allows the simultaneous manipulation of the pump and seed chirps, which can also remarkably benefit the gain bandwidth of the system. The broadband pumped OPA shows potential in generating an intense supercontinuum and few-cycle pulses spanning the whole IR spectral region, which we believe will contribute to the future developments of ultrafast optics and strong field physics.

Author Contributions: Z.H. and Q.Z. wrote the paper, Z.H. and Q.Z. carried out the theoretical investigations, S.A.R. designed the experiments, Z.H. and S.A.R. performed the experiments and the measurements described in the manuscript. All the authors reviewed and provided comments on the manuscript.

Acknowledgments: This work is supported by grant (No. 11574101, 11627809, 11774111) from National Natural Science Foundation of China.

Conflicts of Interest: The authors declare no conflict of interest.

References

1. Brabec, T.; Krausz, F. Intense few-cycle laser fields: Frontiers of nonlinear optics. *Rev. Mod. Phys.* **2000**, *72*, 545–591. [[CrossRef](#)]
2. Krausz, F.; Ivanov, M. Attosecond physics. *Rev. Mod. Phys.* **2009**, *81*, 163–234. [[CrossRef](#)]
3. Itatani, J.; Quere, F.; Yudin, G.L.; Ivanov, M.Y.; Krausz, F.; Corkum, P.B. Attosecond streak camera. *Phys. Rev. Lett.* **2002**, *88*, 173903. [[CrossRef](#)] [[PubMed](#)]

4. Zhang, Q.; Lan, P.; Hong, W.; Liao, Q.; Yang, Z.; Lu, P. The effect of controlling laser field on broadband supercontinuum generation. *Acta Phys. Sin.* **2009**, *58*, 4908–4913.
5. Zhang, Q.; Lu, P.; Hong, W.; Liao, Q.; Lan, P.; Wang, X. Enhanced high-order harmonic generation via controlling ionization in spatially extended systems. *Phys. Rev. A* **2009**, *79*, 053406. [[CrossRef](#)]
6. He, L.; Zhang, Q.; Lan, P.; Cao, W.; Zhu, X.; Zhai, C.; Wang, F.; Shi, W.; Li, M.; Bian, X.-B.; et al. Monitoring ultrafast vibrational dynamics of isotopic molecules with frequency modulation of high-order harmonics. *Nat. Commun.* **2018**, *9*, 1108. [[CrossRef](#)]
7. Zeidler, D.; Staudte, A.; Bardon, A.B.; Villeneuve, D.M.; Dorner, R.; Corkum, P.B. Controlling attosecond double ionization dynamics via molecular alignment. *Phys. Rev. Lett.* **2005**, *95*, 203003. [[CrossRef](#)] [[PubMed](#)]
8. Cao, W.; Laurent, G.; De, S.; Schoffler, M.; Jahnke, T.; Alnaser, A.S.; Bocharova, I.A.; Stuck, C.; Ray, D.; Kling, M.F.; et al. Dynamic modification of the fragmentation of autoionizing states of O-2(+). *Phys. Rev. A* **2011**, *84*, 053406. [[CrossRef](#)]
9. Cao, W.; De, S.; Singh, K.P.; Chen, S.; Schoffler, M.S.; Alnaser, A.S.; Bocharova, I.A.; Laurent, G.; Ray, D.; Zherebtsov, S.; et al. Dynamic modification of the fragmentation of COq+ excited states generated with high-order harmonics. *Phys. Rev. A* **2010**, *82*, 043410. [[CrossRef](#)]
10. Shafir, D.; Soifer, H.; Vozzi, C.; Johnson, A.S.; Hartung, A.; Dube, Z.; Villeneuve, D.M.; Corkum, P.B.; Dudovich, N.; Staudte, A. Trajectory-Resolved Coulomb Focusing in Tunnel Ionization of Atoms with Intense, Elliptically Polarized Laser Pulses. *Phys. Rev. Lett.* **2013**, *111*, 023005. [[CrossRef](#)] [[PubMed](#)]
11. Boge, R.; Cirelli, C.; Landsman, A.S.; Heuser, S.; Ludwig, A.; Maurer, J.; Weger, M.; Gallmann, L.; Keller, U. Probing Nonadiabatic Effects in Strong-Field Tunnel Ionization. *Phys. Rev. Lett.* **2013**, *111*, 103003. [[CrossRef](#)] [[PubMed](#)]
12. Zhang, Q.; Lan, P.; Lu, P. Empirical formula for over-barrier strong-field ionization. *Phys. Rev. A* **2014**, *90*, 043410. [[CrossRef](#)]
13. Cao, W.; Laurent, G.; Ben-Itzhak, I.; Cocke, C.L. Identification of a Previously Unobserved Dissociative Ionization Pathway in Time-Resolved Photospectroscopy of the Deuterium Molecule. *Phys. Rev. Lett.* **2015**, *114*. [[CrossRef](#)] [[PubMed](#)]
14. Hong, Z.; Zhang, Q.; Rezvani, S.A.; Lan, P.; Lu, P. Extending plasma channel of filamentation with a multi-focal-length beam. *Opt. Express* **2016**, *24*, 4029–4041. [[CrossRef](#)] [[PubMed](#)]
15. Zhang, Q.B.; Basnayake, G.; Winney, A.; Lin, Y.F.; Debrah, D.; Lee, S.K.; Li, W. Orbital-resolved nonadiabatic tunneling ionization. *Phys. Rev. A* **2017**, *96*, 023422. [[CrossRef](#)]
16. Chen, Y.; Zhou, Y.; Li, Y.; Li, M.; Lan, P.; Lu, P. Rabi oscillation in few-photon double ionization through doubly excited states. *Phys. Rev. A* **2018**, *97*, 013428. [[CrossRef](#)]
17. Tan, J.; Li, Y.; Zhou, Y.; He, M.; Chen, Y.; Li, M.; Lu, P. Identifying the contributions of multiple-returning recollision orbits in strong-field above-threshold ionization. *Opt. Quant. Electron.* **2018**, *50*, 57. [[CrossRef](#)]
18. Baekhoj, J.E.; Madsen, L.B. Light-induced structures in attosecond transient-absorption spectroscopy of molecules. *Phys. Rev. A* **2015**, *92*, 023407. [[CrossRef](#)]
19. Cao, W.; Warrick, E.R.; Fidler, A.; Leone, S.R.; Neumark, D.M. Near-resonant four-wave mixing of attosecond extreme-ultraviolet pulses with near-infrared pulses in neon: Detection of electronic coherences. *Phys. Rev. A* **2016**, *94*, 021802. [[CrossRef](#)]
20. Cao, W.; Warrick, E.R.; Fidler, A.; Neumark, D.M.; Leone, S.R. Noncollinear wave mixing of attosecond XUV and few-cycle optical laser pulses in gas-phase atoms: Toward multidimensional spectroscopy involving XUV excitations. *Phys. Rev. A* **2016**, *94*, 053846. [[CrossRef](#)]
21. Seres, E.; Seres, J.; Serrat, C.; Namba, S. Core-level attosecond transient absorption spectroscopy of laser-dressed solid films of Si and Zr. *Phys. Rev. B* **2016**, *94*, 165125. [[CrossRef](#)]
22. Shivaram, N.; Tong, X.M.; Timmers, H.; Sandhu, A. Attosecond quantum-beat spectroscopy in helium. *J. Phys. B-Atom. Mol. Opt. Phys.* **2016**, *49*, 055601. [[CrossRef](#)]
23. Cao, W.; Warrick, E.R.; Neumark, D.M.; Leone, S.R. Attosecond transient absorption of argon atoms in the vacuum ultraviolet region: Line energy shifts versus coherent population transfer. *New J. Phys.* **2016**, *18*, 013041. [[CrossRef](#)]
24. Cao, W.; Warrick, E.R.; Fidler, A.; Leone, S.R.; Neumark, D.M. Excited-state vibronic wave-packet dynamics in H-2 probed by XUV transient four-wave mixing. *Phys. Rev. A* **2018**, *97*, 023401. [[CrossRef](#)]
25. Spence, D.E.; Kean, P.N.; Sibbett, W. 60-fsec pulse generation from a self-mode-locked Ti:sapphire laser. *Opt. Lett.* **1991**, *16*, 42–44. [[CrossRef](#)] [[PubMed](#)]

26. Brabec, T.; Spielmann, C.; Curley, P.F.; Krausz, F. Kerr lens mode locking. *Opt. Lett.* **1992**, *17*, 1292–1294. [[CrossRef](#)] [[PubMed](#)]
27. Strickland, D.; Mourou, G. Compression of amplified chirped optical pulses. *Opt. Commun.* **1985**, *55*, 447–449. [[CrossRef](#)]
28. Vaillancourt, G.; Norris, T.B.; Coe, J.S.; Bado, P.; Mourou, G.A. Operation of a 1-kHz pulse-pumped Ti:sapphire regenerative amplifier. *Opt. Lett.* **1990**, *15*, 317–319. [[CrossRef](#)] [[PubMed](#)]
29. Eilanlou, A.A.; Nabekawa, Y.; Ishikawa, K.L.; Takahashi, H.; Midorikawa, K. Direct amplification of terawatt sub-10-fs pulses in a CPA system of Ti:sapphire laser. *Opt. Express* **2008**, *16*, 13431–13438. [[CrossRef](#)]
30. Zhang, Q.; He, L.; Lan, P.; Lu, P. Shaped multi-cycle two-color laser field for generating an intense isolated XUV pulse toward 100 attoseconds. *Opt. Express* **2014**, *22*, 13213–13233. [[CrossRef](#)] [[PubMed](#)]
31. He, L.; Li, Y.; Zhang, Q.; Lu, P. Ultra-broadband water window supercontinuum generation with high efficiency in a three-color laser field. *Opt. Express* **2013**, *21*, 2683–2692. [[CrossRef](#)] [[PubMed](#)]
32. He, M.; Li, Y.; Zhou, Y.; Li, M.; Cao, W.; Lu, P. Direct visualization of valence electron motion using strong-field photoelectron holography. *Phys. Rev. Lett.* **2018**, *120*, 133204. [[CrossRef](#)] [[PubMed](#)]
33. Nikolopoulos, L.A.A. Time-Dependent Theory of Angular Correlations in Sequential Double Ionization. *Phys. Rev. Lett.* **2013**, *111*, 093001. [[CrossRef](#)] [[PubMed](#)]
34. Winney, A.H.; Lee, S.K.; Lin, Y.F.; Liao, Q.; Adhikari, P.; Basnayake, G.; Schlegel, H.B.; Li, W. Attosecond Electron Correlation Dynamics in Double Ionization of Benzene Probed with Two-Electron Angular Streaking. *Phys. Rev. Lett.* **2017**, *119*, 123201. [[CrossRef](#)] [[PubMed](#)]
35. Itatani, J.; Levesque, J.; Zeidler, D.; Niikura, H.; Pepin, H.; Kieffer, J.C.; Villeneuve, D.M. Tomographic imaging of molecular orbitals. *Nature* **2004**, *432*, 867–871. [[CrossRef](#)] [[PubMed](#)]
36. Yuan, H.; He, L.; Wang, F.; Wang, B.; Zhu, X.; Lan, P.; Lu, P. Tomography of asymmetric molecular orbitals with a one-color inhomogeneous field. *Opt. Lett.* **2018**, *43*, 931–934. [[CrossRef](#)] [[PubMed](#)]
37. Zhai, C.; Zhang, X.; Zhu, X.; He, L.; Zhang, Y.; Wang, B.; Zhang, Q.; Lan, P.; Lu, P. Single-shot molecular orbital tomography with orthogonal two-color fields. *Opt. Express* **2018**, *26*, 2775–2784. [[CrossRef](#)] [[PubMed](#)]
38. Wang, B.; He, L.; Wang, F.; Yuan, H.; Zhu, X.; Lan, P.; Lu, P. Resonance-modulated wavelength scaling of high-order-harmonic generation from H_2^+ . *Phys. Rev. A* **2018**, *97*, 013417. [[CrossRef](#)]
39. Baumgartner, R.; Byer, R. Optical parametric amplification. *IEEE J. Quant. Electron.* **1979**, *15*, 432–444. [[CrossRef](#)]
40. Brida, D.; Manzoni, C.; Cirmi, G.; Marangoni, M.; Bonora, S.; Villoresi, P.; De Silvestri, S.; Cerullo, G. Few-optical-cycle pulses tunable from the visible to the mid-infrared by optical parametric amplifiers. *J. Opt.* **2010**, *12*, 013001. [[CrossRef](#)]
41. Cerullo, G.; De Silvestri, S. Ultrafast optical parametric amplifiers. *Rev. Sci. Instrum.* **2003**, *74*, 1. [[CrossRef](#)]
42. Dubietis, A.; Butkus, R.; Piskarskas, A.P. Trends in chirped pulse optical parametric amplification. *IEEE J. Quant. Electron.* **2006**, *12*, 163–172. [[CrossRef](#)]
43. Witte, S.; Eikema, K.S.E. Ultrafast optical parametric chirped-pulse amplification. *IEEE J. Quant. Electron.* **2012**, *18*, 296–303. [[CrossRef](#)]
44. Biegert, J.; Bates, P.K.; Chalus, O. New Mid-Infrared Light Sources. *IEEE J. Quant. Electron.* **2012**, *18*, 531–540. [[CrossRef](#)]
45. Fattahi, H.; Barros, H.G.; Gorjan, M.; Nubbemeyer, T.; Alsaif, B.; Teisset, C.Y.; Schultze, M.; Prinz, S.; Haefner, M.; Ueffing, M.; et al. Third-generation femtosecond technology. *Optica* **2014**, *1*, 45–63. [[CrossRef](#)]
46. Manzoni, C.; Cerullo, G. Design criteria for ultrafast optical parametric amplifiers. *J. Opt.* **2016**, *18*, 103501. [[CrossRef](#)]
47. Limpert, J.; Agueraray, C.; Montant, S.; Hönninger, I.M.; Petit, S.; Descamps, D.; Cormier, E.; Salin, F. Ultra-broad bandwidth parametric amplification at degeneracy. *Opt. Express* **2005**, *13*, 7386–7392. [[CrossRef](#)] [[PubMed](#)]
48. Nikolov, I.; Gaydardzhiev, A.; Buchvarov, I.; Tzankov, P.; Noack, F.; Petrov, V. Ultrabroadband continuum amplification in the near infrared using BiB_3O_6 nonlinear crystals pumped at 800 nm. *Opt. Lett.* **2007**, *32*, 3342–3344. [[CrossRef](#)] [[PubMed](#)]
49. Hädrich, S.; Rothhardt, J.; Röser, F.; Gottschall, T.; Limpert, J.; Tünnermann, A. Degenerate optical parametric amplifier delivering sub 30 fs pulses with 2 GW peak power. *Opt. Express* **2008**, *16*, 19812–19820. [[CrossRef](#)] [[PubMed](#)]

50. Brida, D.; Cirimi, G.; Manzoni, C.; Bonora, S.; Villorresi, P.; De Silvestri, S.; Cerullo, G. Sub-two-cycle light pulses at 1.6 μm from an optical parametric amplifier. *Opt. Lett.* **2008**, *33*, 741–743. [[CrossRef](#)] [[PubMed](#)]
51. Siddiqui, A.M.; Cirimi, G.; Brida, D.; Kärtner, F.X.; Cerullo, G. Generation of <7 fs pulses at 800 nm from a blue-pumped optical parametric amplifier at degeneracy. *Opt. Lett.* **2009**, *34*, 3592–3594. [[CrossRef](#)] [[PubMed](#)]
52. Aguegaray, C.; Schmidt, O.; Rothhardt, J.; Schimpf, D.; Descamps, D.; Petit, S.; Limpert, J.; Cormier, E. Ultra-wide parametric amplification at 800 nm toward octave spanning. *Opt. Express* **2009**, *17*, 5153–5162. [[CrossRef](#)] [[PubMed](#)]
53. Dabu, R. Very broad gain bandwidth parametric amplification in nonlinear crystals at critical wavelength degeneracy. *Opt. Express* **2010**, *18*, 11689–11699. [[CrossRef](#)] [[PubMed](#)]
54. Ishii, N.; Kaneshima, K.; Kitano, K.; Kanai, T.; Watanabe, S.; Itatani, J. Sub-two-cycle, carrier-envelope phase-stable, intense optical pulses at 1.6 μm from a BiB_3O_6 optical parametric chirped-pulse amplifier. *Opt. Lett.* **2012**, *37*, 4182–4184. [[CrossRef](#)] [[PubMed](#)]
55. Hong, K.H.; Lai, C.J.; Siqueira, J.P.; Krogen, P.; Moses, J.; Chang, C.L.; Stein, G.J.; Zapata, L.E.; Kärtner, F.X. Multi-mJ, kHz, 2.1 μm optical parametric chirped-pulse amplifier and high-flux soft x-ray high-harmonic generation. *Opt. Lett.* **2014**, *39*, 3145–3148. [[CrossRef](#)] [[PubMed](#)]
56. Shamir, Y.; Rothhardt, J.; Hädrich, S.; Demmler, S.; Tschernajew, M.; Limpert, J.; Tünnermann, A. High-average-power 2 μm few-cycle optical parametric chirped pulse amplifier at 100 kHz repetition rate. *Opt. Lett.* **2015**, *40*, 5546–5549. [[CrossRef](#)] [[PubMed](#)]
57. Ishii, N.; Kaneshima, K.; Kanai, T.; Watanabe, S.; Itatani, J. Generation of ultrashort intense optical pulses at 1.6 μm from a bismuth triborate-based optical parametric chirped pulse amplifier with carrier-envelope phase stabilization. *J. Opt.* **2015**, *17*, 094001. [[CrossRef](#)]
58. Wilhelm, T.; Piel, J.; Riedle, E. Sub-20-fs pulses tunable across the visible from a blue-pumped single-pass noncollinear parametric converter. *Opt. Lett.* **1997**, *22*, 1494–1496. [[CrossRef](#)] [[PubMed](#)]
59. Shirakawa, A.; Sakane, I.; Takasaka, M.; Kobayashi, T. Sub-5-fs visible pulse generation by pulse-front-matched noncollinear optical parametric amplification. *Appl. Phys. Lett.* **1999**, *74*, 2268. [[CrossRef](#)]
60. Piel, J.; Beutter, M.; Riedle, E. 20–50-fs pulses tunable across the near infrared from a blue-pumped noncollinear parametric amplifier. *Opt. Lett.* **2000**, *25*, 180–182. [[CrossRef](#)] [[PubMed](#)]
61. Huber, R.; Satzger, H.; Zinth, W.; Wachtveitl, J. Noncollinear optical parametric amplifiers with output parameters improved by the application of a white light continuum generated in CaF_2 . *Opt. Commun.* **2001**, *194*, 443–448. [[CrossRef](#)]
62. Kraemer, D.; Hua, R.; Cowan, M.L.; Franjic, K.; Miller, R.J.D. Ultrafast noncollinear optical parametric chirped pulse amplification in KTiOAsO_4 . *Opt. Lett.* **2006**, *31*, 981–983. [[CrossRef](#)] [[PubMed](#)]
63. Tzankov, P.; Zheng, J.; Mero, M.; Polli, D.; Manzoni, C.; Cerullo, G. 300 μJ noncollinear optical parametric amplifier in the visible at 1 kHz repetition rate. *Opt. Lett.* **2006**, *31*, 3629–3631. [[CrossRef](#)] [[PubMed](#)]
64. Zhao, B.; Jiang, Y.; Sueda, K.; Miyanaga, N.; Kobayashi, T. Ultrabroadband noncollinear optical parametric amplification with LBO crystal. *Opt. Express* **2008**, *16*, 18863–18868. [[CrossRef](#)] [[PubMed](#)]
65. Herrmann, D.; Veisz, L.; Tautz, R.; Tavella, F.; Schmid, K.; Pervak, V.; Krausz, F. Generation of sub-three-cycle, 16 TW light pulses by using noncollinear optical parametric chirped-pulse amplification. *Opt. Lett.* **2009**, *34*, 2459–2461. [[CrossRef](#)] [[PubMed](#)]
66. Isaienko, O.; Borguet, E.; Vöhringer, P. High-repetition-rate near-infrared noncollinear ultrabroadband optical parametric amplification in KTiOPO_4 . *Opt. Lett.* **2010**, *35*, 3832–3834. [[CrossRef](#)] [[PubMed](#)]
67. Bromage, J.; Rothhardt, J.; Hädrich, S.; Dorrer, C.; Jocher, C.; Demmler, S.; Limpert, J.; Tünnermann, A.; Zuegel, J.D. Analysis and suppression of parasitic processes in noncollinear optical parametric amplifiers. *Opt. Express* **2011**, *19*, 16797–16808. [[CrossRef](#)] [[PubMed](#)]
68. Huang, S.-W.; Moses, J.; Kärtner, F.X. Broadband noncollinear optical parametric amplification without angularly dispersed idler. *Opt. Lett.* **2012**, *37*, 2796–2798. [[CrossRef](#)] [[PubMed](#)]
69. Darginavičius, J.; Garejev, N.; Dubietis, A. Generation of carrier-envelope phase-stable two optical-cycle pulses at 2 μm from a noncollinear beta-barium borate optical parametric amplifier. *Opt. Lett.* **2012**, *37*, 4805–4807. [[CrossRef](#)] [[PubMed](#)]

70. Zhao, K.; Zhong, H.; Yuan, P.; Xie, G.; Wang, J.; Ma, J.; Qian, L. Generation of 120 GW mid-infrared pulses from a widely tunable noncollinear optical parametric amplifier. *Opt. Lett.* **2013**, *38*, 2159–2161. [[CrossRef](#)] [[PubMed](#)]
71. Nillon, J.; Crégut, O.; Bressler, C.; Haacke, S. Two MHz tunable non collinear optical parametric amplifiers with pulse durations down to 6 fs. *Opt. Express* **2014**, *22*, 14964–14974. [[CrossRef](#)] [[PubMed](#)]
72. Vogelsang, J.; Robin, J.; Piglosiewicz, B.; Manzoni, C.; Farinello, P.; Melzer, S.; Feru, P.; Cerullo, G.; Lienau, C.; Groß, P. High passive CEP stability from a few-cycle, tunable NOPA-DFG system for observation of CEP-effects in photoemission. *Opt. Express* **2014**, *22*, 25295–25306. [[CrossRef](#)] [[PubMed](#)]
73. Schmidt, C.; Bühler, J.; Heinrich, A.-C.; Leitenstorfer, A.; Brida, D. Noncollinear parametric amplification in the near-infrared based on type-II phase matching. *J. Opt.* **2015**, *17*, 094003. [[CrossRef](#)]
74. Hong, Z.; Rezvani, S.A.; Zhang, Q.; Lu, P. Octave-spanning energy-scalable CEP-stabilized pulses from a dual-chirped noncollinear optical parametric amplifier. *Opt. Quant. Electron.* **2017**, *49*, 392. [[CrossRef](#)]
75. Shirakawa, A.; Sakane, I.; Kobayashi, T. Pulse-front-matched optical parametric amplification for sub-10 fs pulse generation tunable in the visible and near infrared. *Opt. Lett.* **1998**, *23*, 1292–1294. [[CrossRef](#)]
76. Baltuska, A.; Fuji, T.; Kobayashi, T. Controlling the carrier-envelope phase of ultrashort light pulses with optical parametric amplifiers. *Phys. Rev. Lett.* **2002**, *88*, 133901. [[CrossRef](#)] [[PubMed](#)]
77. Wang, T.-J.; Major, Z.; Ahmad, I.; Trushin, S.A.; Krausz, F.; Karsch, S. Ultra-broadband near-infrared pulse generation by noncollinear OPA with angular dispersion compensation. *Appl. Phys. B* **2010**, *100*, 207–214. [[CrossRef](#)]
78. Mero, M.; Petrov, V. High-power, few-cycle, angular dispersion compensated mid-infrared pulses from a noncollinear optical parametric amplifier. *IEEE Photon. J.* **2017**, *9*, 3200408. [[CrossRef](#)]
79. Charbonneau-Lefort, M.; Fejer, M.M.; Afeyan, B. Tandem chirped quasi-phase-matching grating optical parametric amplifier design for simultaneous group delay and gain control. *Opt. Lett.* **2005**, *30*, 634–636. [[CrossRef](#)] [[PubMed](#)]
80. Baudisch, M.; Pires, H.; Ishizuki, H.; Taira, T.; Hemmer, M.; Biegert, J. Sub-4-optical-cycle, 340 MW peak power, high stability mid-IR source at 160kHz. *J. Opt.* **2015**, *17*, 094002. [[CrossRef](#)]
81. Baudisch, M.; Hemmer, M.; Pires, H.; Biegert, J. Performance of MgO:PPLN, KTA, and KNbO₃ for mid-wave infrared broadband parametric amplification at high average power. *Opt. Lett.* **2014**, *39*, 5802–5805. [[CrossRef](#)] [[PubMed](#)]
82. Mayer, B.W.; Phillips, C.R.; Gallmann, L.; Keller, U. Mid-infrared pulse generation via achromatic quasi-phase-matched OPCPA. *Opt. Express* **2014**, *22*, 20798–20808. [[CrossRef](#)] [[PubMed](#)]
83. Linnenbank, H.; Linden, S. High repetition rate femtosecond double pass optical parametric generator with more than 2 W tunable output in the NIR. *Opt. Express* **2014**, *22*, 18072–18077. [[CrossRef](#)] [[PubMed](#)]
84. Mayer, B.W.; Phillips, C.R.; Gallmann, L.; Fejer, M.M.; Keller, U. Sub-four-cycle laser pulses directly from a high-repetition-rate optical parametric chirped-pulse amplifier at 3.4 μm . *Opt. Lett.* **2013**, *38*, 4265–4268. [[CrossRef](#)] [[PubMed](#)]
85. Fragemann, A.; Pasiskevicius, V.; Laurell, F. Broadband nondegenerate optical parametric amplification in the mid infrared with periodically poled KTiOPO₄. *Opt. Lett.* **2005**, *30*, 2296–2298. [[CrossRef](#)] [[PubMed](#)]
86. Jovanovic, I.; Brown, C.G.; Ebberts, C.A.; Barty, C.P.J.; Forget, N.; Le Blanc, C. Generation of high-contrast millijoule pulses by optical parametric chirped-pulse amplification in periodically poled KTiOPO₄. *Opt. Lett.* **2005**, *30*, 1036–1038. [[CrossRef](#)] [[PubMed](#)]
87. Brida, D.; Bonora, S.; Manzoni, C.; Marangoni, M.; Villoresi, P.; De Silvestri, S.; Cerullo, G. Generation of 8.5-fs pulses at 1.3 μm for ultrabroadband pump-probe spectroscopy. *Opt. Express* **2009**, *17*, 12510–12515. [[CrossRef](#)] [[PubMed](#)]
88. Jeon, O.-Y.; Jin, M.-J.; Lim, H.-H.; Kim, B.-J.; Cha, M. Broadband optical parametric amplification at the communication band with periodically poled lithium niobate. *Opt. Express* **2006**, *14*, 7210–7215. [[CrossRef](#)] [[PubMed](#)]
89. Deng, Y.; Schwarz, A.; Fattahi, H.; Ueffing, M.; Gu, X.; Ossiander, M.; Metzger, T.; Pervak, V.; Ishizuki, H.; Taira, T.; et al. Carrier-envelope-phase-stable, 1.2 mJ, 1.5 cycle laser pulses at 2.1 μm . *Opt. Lett.* **2012**, *37*, 4973–4975. [[CrossRef](#)] [[PubMed](#)]
90. Fuji, T.; Ishii, N.; Teisset, C.Y.; Gu, X.; Metzger, T.; Baltuska, A.; Forget, N.; Kaplan, D.; Galvanauskas, A.; Krausz, F. Parametric amplification of few-cycle carrier-envelope phase-stable pulses at 2.1 μm . *Opt. Lett.* **2006**, *31*, 1103–1105. [[CrossRef](#)] [[PubMed](#)]

91. Luther, B.M.; Tracy, K.M.; Gerrity, M.; Brown, S.; Krummel, A.T. 2D IR spectroscopy at 100 kHz utilizing a MidIR OPCPA laser source. *Opt. Express* **2016**, *24*, 4117–4127. [[CrossRef](#)] [[PubMed](#)]
92. Marangoni, M.; Osellame, R.; Ramponi, R.; Cerullo, G.; Steinmann, A.; Morgner, U. Near-infrared optical parametric amplifier at 1 MHz directly pumped by a femtosecond oscillator. *Opt. Lett.* **2007**, *32*, 1489–1491. [[CrossRef](#)] [[PubMed](#)]
93. Hong, Z.; Zhang, Q.; Lu, P. Compact dual-crystal optical parametric amplification for broadband IR pulse generation using a collinear geometry. *Opt. Express* **2013**, *21*, 9491–9504. [[CrossRef](#)] [[PubMed](#)]
94. Rezvani, S.A.; Zhang, Q.; Hong, Z.; Lu, P. Tunable broadband intense IR pulse generation at non-degenerate wavelengths using group delay compensation in a dual-crystal OPA scheme. *Opt. Express* **2016**, *24*, 11187–11198. [[CrossRef](#)] [[PubMed](#)]
95. Schmidt, B.E.; Thire, N.; Boivin, M.; Laramée, A.; Poitras, F.; Lebrun, G.; Ozaki, T.; Ibrahim, H.; Legare, F. Frequency domain optical parametric amplification. *Nat. Commun.* **2014**, *5*, 3643. [[CrossRef](#)] [[PubMed](#)]
96. Lassonde, P.; Thire, N.; Arissian, L.; Ernotte, G.; Poitras, F.; Ozaki, T.; Laramée, A.; Boivin, M.; Ibrahim, H.; Legare, F.; et al. High gain frequency domain optical parametric amplification. *IEEE Sel. Top. Quant. Electron.* **2015**, *21*, 8700410. [[CrossRef](#)]
97. Schmidt, B.E.; Béjot, P.; Giguère, M.; Shiner, A.D.; Trallero-Herrero, C.; Bisson, E.; Kasparian, J.; Wolf, J.-P.; Villeneuve, D.M.; Kieffer, J.-C.; Corkum, P.B.; Légaré, F. Compression of 1.8 μm laser pulses to sub two optical cycles with bulk material. *Appl. Phys. Lett.* **2010**, *96*, 121109. [[CrossRef](#)]
98. Thiré, N.; Beaulieu, S.; Cardin, V.; Laramée, A.; Wanie, V.; Schmidt, B.E.; Légaré, F. 10 mJ 5-cycle pulses at 1.8 μm through optical parametric amplification. *Appl. Phys. Lett.* **2015**, *106*, 091110. [[CrossRef](#)]
99. Li, C.; Wang, D.; Song, L.; Liu, J.; Liu, P.; Xu, C.; Leng, Y.; Li, R.; Xu, Z. Generation of carrier-envelope phase stabilized intense 1.5 cycle pulses at 1.75 μm . *Opt. Express* **2011**, *19*, 6783–6789. [[CrossRef](#)] [[PubMed](#)]
100. Mücke, O.D.; Ališauskas, S.; Verhoef, A.J.; Pugžlys, A.; Baltuška, A.; Smilgevičius, V.; Pocius, J.; Giniūnas, L.; Danielius, R.; Forget, N. Self-compression of millijoule 1.5 μm pulses. *Opt. Lett.* **2009**, *34*, 2498–2500. [[CrossRef](#)] [[PubMed](#)]
101. Lu, C.-H.; Tsou, Y.-J.; Chen, H.-Y.; Chen, B.-H.; Cheng, Y.-C.; Yang, S.-D.; Chen, M.-C.; Hsu, C.-C.; Kung, A.H. Generation of intense supercontinuum in condensed media. *Optica* **2014**, *1*, 400–406. [[CrossRef](#)]
102. He, P.; Liu, Y.; Zhao, K.; Teng, H.; He, X.; Huang, P.; Huang, H.; Zhong, S.; Jiang, Y.; Fang, S.; et al. High-efficiency supercontinuum generation in solid thin plates at 0.1 TW level. *Opt. Lett.* **2017**, *42*, 474–477. [[CrossRef](#)] [[PubMed](#)]
103. Rudd, J.V.; Law, R.J.; Luk, T.S.; Cameron, S.M. High-power optical parametric chirped-pulse amplifier system with a 1.55 μm signal and a 1.064 μm pump. *Opt. Lett.* **2005**, *30*, 1974–1976. [[CrossRef](#)] [[PubMed](#)]
104. Kraemer, D.; Cowan, M.L.; Hua, R.; Franjic, K.; Dwayne Miller, R.J. High-power femtosecond infrared laser source based on noncollinear optical parametric chirped pulse amplification. *J. Opt. Soc. Am. B* **2007**, *24*, 813–818. [[CrossRef](#)]
105. Moses, J.; Manzoni, C.; Huang, S.-W.; Cerullo, G.; Kärtner, F.X. Temporal optimization of ultrabroadband high-energy OPCPA. *Opt. Express* **2009**, *17*, 5540–5555. [[CrossRef](#)] [[PubMed](#)]
106. Takahashi, E.J.; Kanai, T.; Nabekawa, Y.; Midorikawa, K. 10mJ class femtosecond optical parametric amplifier for generating soft xray harmonics. *Appl. Phys. Lett.* **2008**, *93*, 041111. [[CrossRef](#)]
107. Zhang, Q.; Takahashi, E.J.; Mücke, O.D.; Lu, P.; Midorikawa, K. Dual-chirped optical parametric amplification for generating few hundred mJ infrared pulses. *Opt. Express* **2011**, *19*, 7190–7212. [[CrossRef](#)] [[PubMed](#)]
108. Fu, Y.X.; Takahashi, E.J.; Xue, B.; Midorikawa, K. Generation of a 200-mJ class infrared femtosecond laser by dual-chirped optical parametric amplification. In Proceedings of the Conference on Lasers And Electro-Optics (Cleo), San Jose, CA, USA, 14–19 May 2017.
109. Hong, Z.; Zhang, Q.; Rezvani, S.A.; Lan, P.; Lu, P. Tunable few-cycle pulses from a dual-chirped optical parametric amplifier pumped by broadband laser. *Opt. Laser Technol.* **2018**, *98*, 169–177. [[CrossRef](#)]
110. Hong, Z.; Zhang, Q.; Lan, P.; Lu, P. Generation of few-cycle infrared pulses from a degenerate dual-pump OPCPA. *Opt. Express* **2014**, *22*, 5544–5557. [[CrossRef](#)] [[PubMed](#)]
111. Zeng, S.; Zhang, B.; Dan, Y.; Li, X.; Sun, N.; Sui, Z. Analysis and optimization of chirp-compensation OPCPA scheme. *Opt. Commun.* **2010**, *283*, 4054–4058. [[CrossRef](#)]
112. Tang, Y.; Ross, I.N.; Hernandez-Gomez, C.; New, G.H.C.; Musgrave, I.; Chekhlov, O.V.; Matousek, P.; Collier, J.L. Optical parametric chirped-pulse amplification source suitable for seeding high-energy systems. *Opt. Lett.* **2008**, *33*, 2386–2388. [[CrossRef](#)] [[PubMed](#)]

113. Yin, Y.; Li, J.; Ren, X.; Wang, Y.; Chew, A.; Chang, Z. High-energy two-cycle pulses at 3.2 μm by a broadband-pumped dual-chirped optical parametric amplification. *Opt. Express* **2016**, *24*, 24989–24998. [[CrossRef](#)] [[PubMed](#)]
114. Yin, Y.; Li, J.; Ren, X.; Zhao, K.; Wu, Y.; Cunningham, E.; Chang, Z. High-efficiency optical parametric chirped-pulse amplifier in BiB_3O_6 for generation of 3 mJ, two-cycle, carrier-envelope-phase-stable pulses at 1.7 μm . *Opt. Lett.* **2016**, *41*, 1142–1145. [[CrossRef](#)] [[PubMed](#)]
115. Xu, J.; Kawano, H.; Liu, W.; Hanada, Y.; Lu, P.; Miyawaki, A.; Midorikawa, K.; Sugioka, K. Controllable alignment of elongated microorganisms in 3D microspace using electrofluidic devices manufactured by hybrid femtosecond laser microfabrication. *Microsyst. Nanoeng.* **2017**, *3*, 16078. [[CrossRef](#)]
116. Qin, C.; Zhou, F.; Peng, Y.; Sounas, D.; Zhu, X.; Wang, B.; Dong, J.; Zhang, X.; Alù, A.; Lu, P. Spectrum control through discrete frequency diffraction in the presence of photonic gauge potentials. *Phys. Rev. Lett.* **2018**, *120*, 133901. [[CrossRef](#)] [[PubMed](#)]
117. Li, Y.; Chen, W.; Wang, H.; Liu, N.; Lu, P. Bragg gratings in all-solid Bragg photonic crystal fiber written with femtosecond pulses. *J. Lightw. Technol.* **2011**, *29*, 3367–3371. [[CrossRef](#)]
118. Ma, X.; Li, M.; Zhou, Y.; Lu, P. Nonsequential double ionization of Xe by mid-infrared laser pulses. *Opt. Quant. Electron.* **2017**, *49*, 170. [[CrossRef](#)]
119. Hou, M.; Wang, Y.; Liu, S.; Li, Z.; Lu, P. Multi-components interferometer based on partially filled dual-core photonic crystal fiber for temperature and strain sensing. *IEEE Sens. J.* **2016**, *16*, 6192–6196. [[CrossRef](#)]
120. Tsai, T.; Chang, C.; Gwo, S. Ultrafast hot electron relaxation time anomaly in InN epitaxial films. *Appl. Phys. Lett.* **2007**, *90*, 252111. [[CrossRef](#)]
121. Tsai, T.; Chang, C.; Kuo, C.; Hwang, J.; Lin, T.; Gwo, S. Spectral dependence of time-resolved photoreflectance of InN epitaxial films. *Appl. Phys. Lett.* **2009**, *95*, 142108. [[CrossRef](#)]
122. Mohanta, A.; Jang, D.; Wang, M.; Tu, L. Time-integrated photoluminescence and pump-probe reflection spectroscopy of Si doped InN thin films. *J. Appl. Phys.* **2014**, *115*, 044906. [[CrossRef](#)]



© 2018 by the authors. Licensee MDPI, Basel, Switzerland. This article is an open access article distributed under the terms and conditions of the Creative Commons Attribution (CC BY) license (<http://creativecommons.org/licenses/by/4.0/>).